ADVANCED THEORY AND SIMULATIONS
www.advtheorysimul.com

Wideband Epsilon-Near-Zero Supercoupling Control through Substrate-Integrated Impedance Surface

Yijing He, Yue Li, Ziheng Zhou, Hao Li, Yuefeng Hou, Shaolin Liao, and Pai-Yen Chen*

The supercoupling phenomenon of electromagnetic wave through arbitrary shaped epsilon-near-zero (ENZ) material channels has attracted considerable attention recently, leading to numerous intriguing applications. It has been demonstrated that around the cutoff frequency of fundamental TE_{10} mode, waveguide behaves as the 2D homogenous ENZ material. However, for a given waveguide geometry, the ENZ operating bandwidth is inherently narrow and the center frequency is fixed. Here, a reconfigurable ENZ medium is proposed and experimentally demonstrated with a wideband-tunable supercoupling effect by means of inserting a metasurface inside the waveguide, named as substrate-integrated impedance surface (SIIS). With different insertion depth (which can be mechanically tuned) of SIIS, the ENZ supercoupling frequency can be precisely controlled. The proposed technique not only achieves wideband tuning of the ENZ supercoupling, especially to control the enhanced group delay of the electromagnetic waves, thereby offering a promising way toward for tunable slow-light devices, such as light storage and processing components.

Recently, metamaterials with specifically tailored permittivity ε or permeability μ have attracted considerable attention due to their anomalous features and properties in controlling the propagation of electromagnetic wave. These artificial electromagnetic materials have been widely applied to microwave absorbers, antennas, sensors, and so on.[1–3] Epsilon-near-zero (ENZ) material has becomes a widely studied topic from optics to microwaves.[4,5] When electromagnetic wave propagates along the ENZ material, its effective wavelength and effective phase velocity are infinite. Owing to this intriguing property, ENZ material has enabled many exotic applications in radiation pattern tailoring,[6–8] cloaking devices,[9,10] subwavelength imaging,[11,12] Purcell enhancement,[13,14] enhanced nonlinearities,[15–17] optical nanocircuits,[18–20] and macroscopic photonic doping,[21] to name a few.

As one of the anomalous applications of ENZ materials, electromagnetic wave supercoupling has received extensive attention.[22–26] In 2006, Silveirinha and Engheta discovered the "supercoupling" of guided electromagnetic waves through an ultranarrow arbitrary-shaped channel filled with ENZ material.[22] Despite of the large geometric (impedance) mismatch between the external waveguides and the narrow channel, full transmission can be achieved at the supercoupling frequency, at which the effective permittivity of the narrow channel is close to zero. This phenomenon has been theoretically studied and experimentally verified using a microwave waveguide operating near the cutoff frequency of the TE_{10} mode (fundamental mode).[25] Due to the inherent fixed cutoff frequency and narrow ENZ operating bandwidth of a metallic waveguide, the supercoupling effect works only for a fixed and narrow frequency range. So far, several methods have been proposed to achieve the tunability of the ENZ supercoupling frequency. For example, nonlinear control of the ENZ supercoupling was achieved using a varactor diode placed in the middle of the narrow waveguide channel.[27] The reduction of transmission amplitude and quality factor Q happened due to the parasitic effect of loaded varactors. In another method, two longitudinal slots with variable length achieved by pin diodes were etched on the broadside of the narrow channel, in order to achieve the tuning of ENZ supercoupling frequency.[28] However, these loaded slots could result in considerable radiation leakages and thus increase the propagation loss.

In this work, we introduce a metasurface loading technique to achieve the wideband control of the waveguide-based ENZ supercoupling, as illustrated in **Figure 1**. The middle ultra-narrow waveguide channel connecting the two external feeding waveguides is loaded with a properly designed metasurface, which is constituted by periodically positioned blind vias array, and named as substrate-integrated impedance surface (SIIS). In this case, the SIIS provides a homogenous and capacitive impedance of $Z_s = i/\omega C_s$, where C_s is surface capacitance and ω is the radian frequency. The SIIS 1 and SIIS 2 in Figure 1 are with different insertion depths in the narrow channel. By varying the insertion depth of SIIS, wideband control of ENZ supercoupling with high

Y. He, Prof. Y. Li, Z. Zhou, H. Li, Y. Hou
Department of Electronic Engineering
Tsinghua University
Beijing 100084, China
E-mail: lyee@tsinghua.edu.cn
Dr. S. Liao
Argonne National Laboratory
Lemont, IL 60439, USA
Prof. P.-Y. Chen
Department of Electrical and Computer Engineering
University of Illinois at Chicago
Chicago, IL 60607, USA

The ORCID identification number(s) for the author(s) of this article can be found under https://doi.org/10.1002/adts.201900059

DOI: 10.1002/adts.201900059

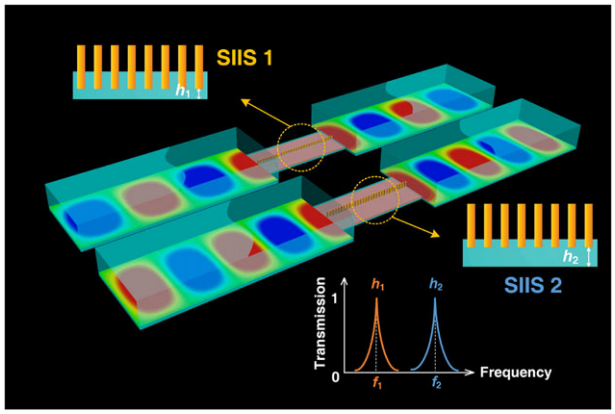

Figure 1. The general idea to achieve wideband epsilon-near-zero supercoupling control using the SIIS structure: The picture gives the comparison of the ENZ supercoupling phenomenon at two different frequencies utilizing the proposed SIIS. The two waveguide systems have identical set up apart from the middle narrow channel, which are loaded with the SIIS in different insertion depths. By changing the insertion depth of the SIIS, wideband epsilon-near-zero (ENZ) supercoupling control can be realized.

transmittance can be achieved, thanks to the capacitive and non-resonant nature of the SIIS. The wideband tuning of the ENZ supercoupling and the associated slow-light effect could enable many new applications in sensing, communication, and information storage and processing.

It is known that a rectangular metallic waveguide operating in fundamental TE_{10} mode has the propagation constant $\beta = \sqrt{(2\pi nf/c)^2 - (\pi/w)^2}$, where w is the width of waveguide, n is the relative refractive index of the dielectric filled in the waveguide, c is the light velocity in vacuum, and f is the operating frequency. The effective permittivity and permeability for the waveguide in TE_{10} mode can be written as,[25]

$$\varepsilon_{eff}/\varepsilon_0 = \varepsilon_r - c^2/4f^2w^2 \quad (1)$$

$$\mu_{eff} = \mu_0 \quad (2)$$

where ε_0 and μ_0 are the free-space permittivity and permeability, ε_r is the relative permittivity of the dielectric filling the waveguide, c is the velocity of light in vacuum, w is the width of the waveguide. Here, time convention $e^{-i\omega t}$ is assumed throughout this paper. It can be determined that at cutoff frequency $f = c/(2w\sqrt{\mu\varepsilon_r})$, effective permittivity $\varepsilon_{eff} = 0$, that is, the waveguide can emulate ENZ material near the cutoff frequency.

When an ideal lossless ENZ material is inserted within the channel to form the waveguide-ENZ-waveguide sandwich structure, the reflection coefficient at the input transition can be written as,[23]

$$R = \frac{ik_0\mu_0 A}{2h - ik_0\mu_0 A} \quad (3)$$

where $k_0 = 2\pi f/c$ is the wave number in free-space and A is the total longitudinal cross-section area of the channel filled with the ENZ material. From Equation (3), it can be observed that only when A is small, the reflection coefficient R can become near zero.[23]

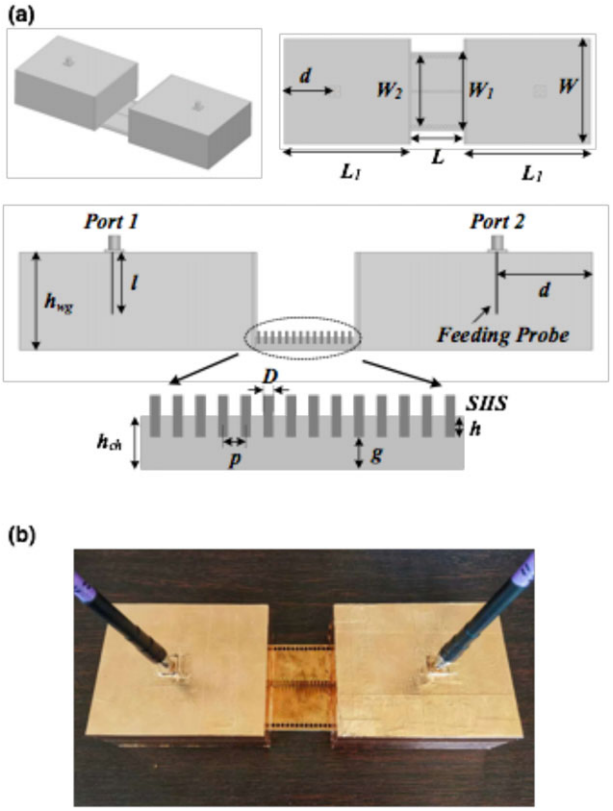

Figure 2. The proposed structure to achieve wideband control of ENZ supercoupling: a) The perspective view, top view, and cross-section view of the experimental setup. The external input and output waveguides are connected using a narrow waveguide channel with different H-plane width. Moreover, all the geometric parameters are listed here, $W = 100$ mm, $d = 48$ mm, $W_1 = 75$ mm, $W_2 = 67$ mm, $h_{ch} = 2$ mm, $D = 2r = 2.0$ mm, $s = 3.8$ mm, $l = 31$ mm, $p = 3$ mm, $h_{wg} = 50$ mm, $L = 50$ mm, $L_1 = 120$ mm. b) The fabricated prototype to perform the experiment: The input and output waveguides are fed using two standard 50-Ω coaxial probes.

Figure 2a illustrates one of many possible SIIS structures constituted by an array of subwavelength periodically-arranged blind vias. The gap between the SIIS and the bottom plate of the narrow channel is denoted as g, the period of SIIS represented as p, and the radius of blind vias is indicated as a. The surface impedance and the capacitance of the SIIS can be derived (detailed in Supporting Information) and expressed as[29]

$$Z_s = -\frac{1}{i\omega C_s},\ C_s = \frac{\frac{\varepsilon}{d_x d_y}}{\frac{3[\ln(2h/a)-1]}{4\pi h^3} - \frac{c}{(d_x d_y)^{3/2}}} \quad (4)$$

where the $d_x = p$, $d_y = 2h + g$, a is the radius of the metallic wires, c is an empirical fitting parameter, ε is the permittivity of the dielectric. From Equation (4), it can be observed that by changing the insertion depth of the SIIS, the surface capacitance C_s can be manipulated. The smaller gap size g or period p of the SIIS can lead to the larger values of the surface capacitance C_s. In addition, when a SIIS is inserted in the middle plane of the waveguide, the

waveguide dispersion characteristics can be tailored according to the following dispersion relationship[29]

$$\frac{-i\omega\mu_0}{2\sqrt{k^2-\beta^2}}\tan\left[\sqrt{k^2-\beta^2}\frac{w}{2}\right]-\frac{1}{i\omega C_s}=0 \tag{5}$$

When the SIIS-loaded narrow waveguide works around cutoff frequency ω_c, that is, the propagation constant of the narrow waveguide $\beta(\omega_c)\approx 0$, we can get the following relationship between the cutoff frequency and the desired surface capacitance from Equation (5),

$$C_s \approx \frac{2}{\omega_c\sqrt{\frac{\mu_0}{\varepsilon}}\tan(\omega_c\sqrt{\varepsilon\mu_0}\frac{w}{2})} \tag{6}$$

It can be seen that the lower cutoff frequency ω_c of the waveguide requires the larger values of the surface capacitance C_s. Because the surface capacitance C_s of the SIIS has a strong function with the gap size g and the period p, the cutoff frequency ω_c of the SIIS-loaded narrow waveguide channel can be tailored by just controlling the gap size g or the period p of the SIIS. When the period p is fixed, just by selecting the proper values of gap size g of the embedded impedance surface, the desired surface capacitance C_s for a specifically reduced cutoff frequency ω_c of the narrow waveguide channel can be obtained. When the SIIS-loaded narrow waveguide channel operates at the cutoff frequency ω_c, it effectively behaves as an ENZ material. As a result, the ENZ supercoupling occurs at the cutoff frequency of the narrow waveguide channel. Wideband ENZ supercoupling frequency control can be achieved between the two cutoff frequencies of the external waveguide and the narrow waveguide channel.

Here, we demonstrate the wideband control of the ENZ-based supercoupling sandwich structure numerically and experimentally. The structure consists of three regions, including the two input and output waveguides, and the narrow waveguide channel [Figure 2a]. The external waveguides are filled with Teflon ($\varepsilon_r = 2.1$). The width and height of the external waveguides are $W = 100$ mm and $h = 50$ mm, respectively, resulting in the cutoff frequency $f_0 = 1.03$ GHz. The middle region connecting the external input and output waveguides is a narrow waveguide channel filled with dielectric substrate F4B, whose permittivity $\varepsilon_r = 2.2$ and loss tangent $\tan\delta = 0.002$. It is noted here that the middle narrow channel is fabricated using the standard printed circuit board (PCB) technology. The width and thickness of the middle dielectric substrate are $W_1 = 75$ mm and $h_{ch} = 2$ mm, respectively. The two arrays of via holes are drilled in the dielectric substrate with a distance of $W_2 = 67$ mm to form the sidewalls of substrate integrated waveguide (SIW) narrow channel.[30] The cutoff frequency of the pure SIW (i.e., without loading the SIIS) is around $f_1 = 1.55$ GHz. The diameter and pitch of the sidewall vias are $D_1 = 3.0$ mm and $s = 3.8$ mm, respectively. The SIIS is formed by arranging an array of metal blind vias along the middle longitudinal plane of the SIW with subwavelength spacing, by means of the identical mechanical drilling process.

Both the input and output waveguides are excited using the standard 50-Ω coaxial feeding probe. The distance between the feeding probe and the shorted waveguide wall is set to be d and the length of the feeding probe is l. It is noted that both parameters d and l have great influence on the impedance matching for the coaxial-to-waveguide transitions. In addition, the sharp abrupt in E-plane, that is, the E-plane discontinuity, can be modeled as a shunt capacitance. Meanwhile the H-plane width difference between the external feeding waveguides and narrow channel, that is, the H-plane discontinuity, can be modeled as a shunt inductor.[31] Here, it is worth mentioning that the E-plane and H-plane steps have a negligible effect on the supercoupling properties because the associated propagation at the supercoupling frequency is static-wise in nature.[23] In addition, at low frequencies, ignoring higher-order Floquet modes, the proposed SIIS can be modeled as a capacitive impedance sheet (or a surface capacitance C_s). To validate the proposed method, we have fabricated a prototype of the proposed structure, which is shown in Figure 2b.

The simulated and measured results are depicted in **Figure 3**. The numerical results presented here are obtained using the frequency-domain finite-element method.[32] The scattering parameters were measured using an Agilent ENA-5071B Network Analyzer. Here, the period of the SIIS is fixed to $p = 3$ mm, the radius of these blind vias is fixed to $r = 1$ mm. Figure 3a shows the simulated transmission amplitudes between two feeding ports under different g. The two dashed lines denote the transmission amplitude of the single external feeding waveguide and single narrow waveguide channel respectively. The dotted lines represent the simulated transmission amplitude between the two feeding ports. The first transmission peak represents the ENZ supercoupling. The transmission peak occurs at higher frequency and is due to the classic Fabry–Pérot (FP) resonance, which strongly depends on the length of the waveguide channel. More specifically, FP resonance satisfies the relationship $\tan(\beta_{ch}l) = 0$, β_{ch} is the propagation constant inside the narrow waveguide channel at resonant frequency, and l is the length of the channel. The most remarkable difference between the ENZ supercoupling and FP resonance lies in the phase and amplitude distribution along the narrow waveguide channel. For ENZ supercoupling, there is almost no phase variation inside the narrow waveguide channel, and the amplitude of the electric field is also near uniform. While at FP resonance, there exists a strong standing wave distribution along the waveguide channel. Hence, FP resonance provides a 180° phase shift and non-uniform magnitude distribution between the entrance and the exit of the narrow waveguide channel.[23]

It is clearly seen that wideband control of ENZ supercoupling frequency can be achieved within the two cutoff frequencies. Even more remarkably, high and stable transmission amplitude can be maintained across the wide tuning range. Figure 3b shows the comparison between the simulated and measured transmission coefficients with different g. The dotted lines represent the simulated results, and the solid lines are the measured ones, which agree well with each other. It can be seen that when $g = 2$ mm (i.e., a regular SIW without loading SIIS), the measured supercoupling frequency occurs around 1.55 GHz, which is identical with the theoretical cutoff frequency of the narrow channel. When g is reduced to 0.5 mm, the measured supercoupling frequency moves down to 1.44 GHz. When g is further reduced to 0.2 mm, the supercoupling frequency becomes 1.31 GHz. The measured results are consistent with the simulated results, except for slight discrepancy in magnitude of transmission coefficient. This is mainly due to impedance mismatch

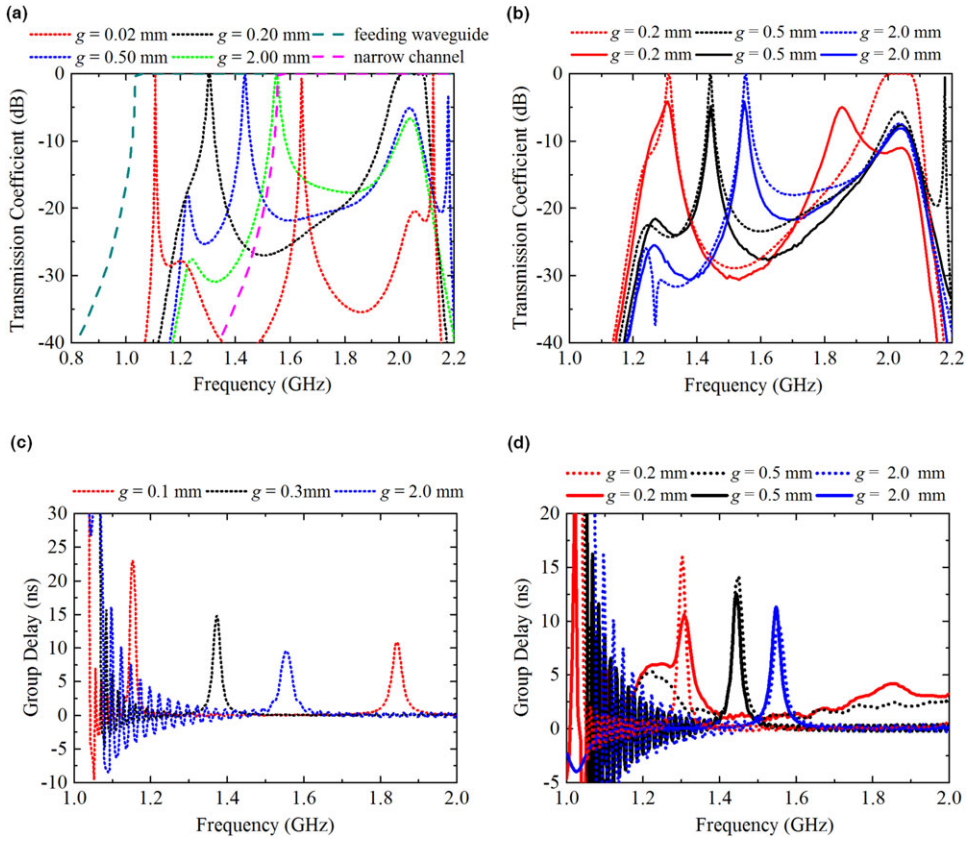

Figure 3. The simulated and measured transmission amplitude and group delay of the SIIS-loaded ENZ waveguide with different g. a) The simulated transmission amplitude of the SIIS-loaded ENZ waveguide with different g (the two high-pass dashed lines represent the transmission coefficients of the external waveguides and the narrow channel respectively). b) The simulated and measured transmission amplitude when the SIIS-loaded narrow waveguide channel are with different g (the dotted lines represent the simulated results and solid lines represent the measured ones). c) The simulated group delays of electromagnetic wave tunneling through the SIIS-loaded ENZ waveguide with different g. d) The simulated and measured group delays of electromagnetic wave tunneling through the SIIS-loaded narrow waveguide channel with different g (the dotted lines represent the simulated results and solid lines represent the measured ones).

between coaxial probes and external waveguides, and fabrication errors.

In addition, it is known that group velocity and group delay are the two important parameters in communication systems. The two parameters reflect the propagation velocity of a packet of electromagnetic waves with finite bandwidth in media. Here, we also discuss the group delay of the electromagnetic wave through the ENZ channel. The group velocity and group delay are given by

$$v_g = \frac{d\omega}{d\beta},\ n_g = -\frac{d\beta}{d\omega} \tag{7}$$

As the wavelength and phase velocity exhibit infinite property in ENZ material, electromagnetic wave demonstrates correspondingly a very low group velocity, thus a large group delay in ENZ material. We have simulated and measured the group delay of the system using the transmission phase variation across the narrow waveguide channel. Figure 3c studies the relationship between the simulated group delay with the SIIS under different g. It is evident that the group delay increases with the reduction of g. Figure 3d shows the comparison between the simulated and measured group delays with different g. The dotted lines represent the simulated group delay, and the solid lines denote the measured ones. It can be clearly seen that the frequency where the maximum group delay happens corresponds to peak frequency of ENZ supercoupling. The simulated and measured peak frequency agree well with each other. The slight differences in amplitudes for $g = 0.2$ mm are mainly due to the fabrication and assembly errors of system. From the results of Figure 3c,d, the proposed SIIS can enhance the group delay of waveguide. This intriguing property can be used to reduce the speed of light propagation. Slowing down light can increase its interaction time with loaded materials, devices, or circuits, thus enhancing, for instance, the effective nonlinearity for many switching, wave-mixing, and frequency-conversion applications. In the realm of quantum computing, this phenomenon can offer a promising avenue toward slowing light for information storage and processing.[33]

Figure 4a presents the simulated transmission coefficients with the different lengths L of the narrow waveguide channel; here, the geometric parameters of SIIS are fixed to: $g = 0.5$ mm, $p = 3$ mm, and $r = 1$ mm. From Figure 4a, it is seen that when the SIIS-loaded narrow waveguide channel is with different

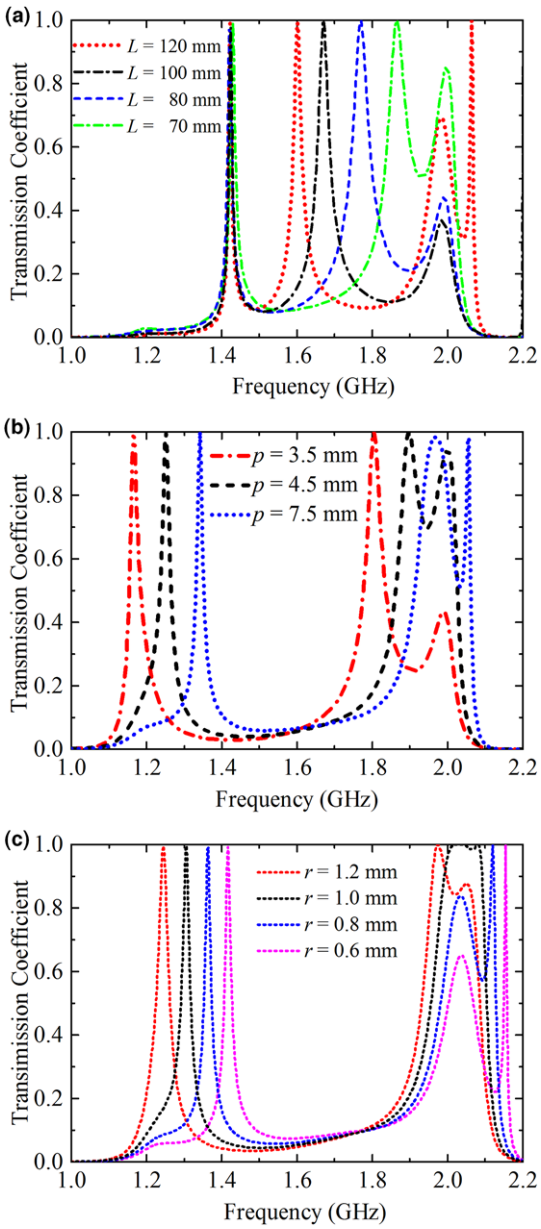

Figure 4. Parameter studies of the SIIS-loaded narrow waveguide channel. a) The simulated transmission amplitude of the SIIS-loaded narrow waveguide channel with different lengths *L*. b) The simulated transmission amplitude of the SIIS-loaded narrow waveguide channel with different period *p*. c) The simulated transmission amplitude of the SIIS-loaded narrow waveguide channel with different radius *r*.

length *L*, the supercoupling frequency remains unchanged and independent of the channel length *L*. Moreover, FP resonance occurs at the higher frequencies, for which the frequency changes inversely with the length *L* of the channel. Figure 4b shows the simulated transmission coefficient for the SIIS-loaded narrow channel with different *p*. It can be observed that when *p* decreases, both the ENZ supercoupling frequency and FP resonance frequency are simultaneously shifted to lower frequency. The simulated transmission coefficients for the SIIS-loaded narrow waveguide channel with different via radius *r* are shown in Figure 4c. From the figure, when *r* increases, supercoupling frequency is reduced. From Equation (4), larger radius *r* of the blind vias can lead to larger surface capacitance C_s of the SIIS, thus resulting in the reduction of the supercoupling frequency. In addition, nearly full transmission amplitude can be maintained across the whole tuning range. In addition, the effect of the dielectric loss inside the narrow waveguide channel on the ENZ supercoupling has been discussed in Supporting Information.

In this work, we have theoretically and experimentally demonstrated a SIIS-loading technique, which enables a new mechanism to achieve wideband control of the ENZ supercoupling frequency. By mechanically varying insertion depth of the SIIS in waveguide, ENZ supercoupling with nearly full transmission across the whole tuning range can be achieved, due to the non-resonant nature of the reactive SIIS. The proposed reconfigurable ENZ structure could open up many exciting applications, such as enhanced optical nonlinearities for wave mixing,[34] high-gain antennas,[35] and even quantum information storage and processing,[36] due to the enhanced group delay of the ENZ structure.

Experimental Section

Numerical Simulation: The numerical results presented in this work were obtained using the commercial software CST Microwave Studio, which is a general purpose time-domain Maxwellian solver based on the finite integration technique (FIT). In the simulations, PEC, metals, and dielectrics are described by realistic material models (including dispersion, conductivity, and loss tangent). The lumped port was chosen as the excitation source for the 50-Ω coaxial feed.

Fabrication of Experimental Device: The two external waveguides are made by covering the copper sheet on the surfaces of the two identical Teflon cuboids with permittivity of 2.1, both of which have a volume of $100 \times 120 \times 50$ mm^3. The middle region is a narrow substrate-integrated waveguide (SIW) channel loaded with the impedance surface. The SIW and impedance surface were fabricated using the standard PCB process. The dielectric substrate is the F4B with permittivity of 2.2 and thickness of 2 mm. The conducting via holes are drilled in the dielectric substrate with a distance of 67 mm to form the two sidewalls of SIW. The SIIS was fabricated using the same mechanical drilling process. Because these three parts are fabricated independently, they have to be assembled together finally. In addition, it is noted that the width of external waveguide and the middle channel are not same. The copper foil is utilized to achieve good electric connection between the SIW channel and the two external waveguides. The copper foils are bent and wrapped well on the connection between the two E and H-plane steps to ensure good transmission between the external waveguide and the middle channel.

Measurement Setup for Reflection Coefficients and Group Delay: The transmission coefficient and the group delay were measured using a vector network analyzer (Aglient N5071B), over the frequency range 300KHz–8 GHz. The device under test (DUT) was connected with the vector network analyzer using two coaxial cables (ST18-SMSM-1M). The vector network analyzer was calibrated using Electronic Calibration Module 85093C.

Acknowledgements

This work was supported by the National Natural Science Foundation of China 61771280.

Conflict of Interest

The authors declare no conflict of interest.

Keywords

epsilon-near-zero, group delay control , slow electromagnetic wave, super-coupling effect, waveguide integrated metasurface

Received: March 25, 2019
Revised: April 28, 2019
Published online:

[1] N. I. Landy, S. Sajuyigbe, J. J. Mock, D. R. Smith, W. J. Padilla, *Phys. Rev. Lett.* **2008**, *100*, 207402.
[2] E. Ekmekci, G. Turhan-Sayan, *Appl. Phys. A* **2013**, *110*, 189.
[3] J. Zhu, G. V Eleftheriades, *IEEE Antennas Wireless Propag. Lett.* **2009**, *8*, 1259.
[4] N. Engheta, *Science* **2013**, *340*, 286.
[5] I. Liberal, N. Engheta, *Nat. Photonics* **2017**, *11*, 149.
[6] S. Enoch, G. Tayeb, P. Sabouroux, N. Guérin, P. Vincent, *Phys. Rev. Lett.* **2002**, *89*, 213902.
[7] R. W. Ziolkowski, *Phys. Rev. E* **2004**, *70*, 46608.
[8] A. Alù, M. G. Silveirinha, A. Salandrino, N. Engheta, *Phys. Rev. B* **2006**, *75*, 1418.
[9] M. G. Silveirinha, A. Alù, N. Engheta, *Phys. Rev. E* **2007**, *75*, 36603.
[10] B. Edwards, A. Alù, M. G. Silveirinha, N. Engheta, E. Brian, *Phys. Rev. Lett.* **2009**, *103*, 153901.
[11] A. Salandrino, N. Engheta, *Phys. Rev. B* **2006**, *74*, 075103.
[12] G. Castaldi, S. Savoia, V. Galdi, A. Alù, N. Engheta, *Phys. Rev. B* **2012**, *86*, 115123.
[13] A. Alù, N. Engheta, *Phys. Rev. Lett.* **2009**, *103*, 43902.
[14] A. V Chebykin, A. A. Orlov, A. S. Shalin, A. N. Poddubny, P. A. Belov, *Phys. Rev. B* **2015**, *91*, 205126.
[15] M. Z. Alam, L. I. De, R. W. Boyd, *Science* **2016**, *352*, 795.
[16] A. Capretti, Y. Wang, N. Engheta, L. D. Negro, *ACS Photonics* **2015**, *2*, 1584.
[17] C. Argyropoulos, P. Y. Chen, G. D'Aguanno, N. Engheta, A. Alù, *Phys. Rev. B* **2012**, *85*. 045129.
[18] N. Engheta, A. Salandrino, A. Alù, *Phys. Rev. Lett.* **2005**, *95*, 95504.
[19] N. Engheta, *Science* **2007**, *317*, 1698.
[20] Y. Li, I. Liberal, C. D. Giovampaola„ N. Engheta, *Sci. Adv.* **2016**, *2*, e1501790.
[21] I. Liberal, A. M. Mahmoud, Y. Li, B. Edwards, N. Engheta, *Science* **2017**, *355*, 1058.
[22] M. G. Silveirinha, N. Engheta, *Phys. Rev. B* **2007**, *76*, 245109.
[23] A. Alù, M. G. Silveririnha„ N. Engheta, *Phys. Rev. E* **2008**, *78*, 16604.
[24] A. Alù, N. Engheta, *Phys. Rev. B* **2008**, *78*, 1436.
[25] B. Edwards, A. Alù, M. E. Young, M. Silveirinha, N. Engheta, *Phys. Rev. Lett.* **2008**, *100*, 033903.
[26] Y. Li, N. Engheta, *Phys. Rev. B* **2014**, *90*. 201107.
[27] D. A. Powell, A. Alù, B. Edwards, A. Vakil, Y. S. Kivshar, N. Engheta, *Phys. Rev. B* **2009**, *79*, 245135.
[28] M. Mitrovic, B. Jokanovic, N. Vojnovic, *IEEE Antennas Wireless Propag. Lett.* **2013**, *12*, 631.
[29] Y. He, Y. Li, L. Zhu, H. Bagci, D. Erricolo, P. Y. Chen, *Phys. Rev. Appl.* **2018**, *10*, 064024.
[30] D. Deslandes, K. Wu, *IEEE Trans. Microwave Theory Tech.* **2006**, *54*, 2516.
[31] R. E. Collin, *Field Theory of Guided Waves*, 2nd ed., IEEE Press, New York **1991**.
[32] CST Microwave Studio, Feb 2016, www.cst.com.
[33] G. D'Aguanno, N. Mattiucci, M. J. Bloemer, R. Trimm, N. Aközbek, A. Alù, *Phys. Rev. B* **2014**, *90*, 54202.
[34] A. Capretti, Y. Wang, N. Engheta, L. D.Negro, *Opt. Lett.* **2015**, *40*, 1500.
[35] A. Alù, M. G. Silveirinha, A. Salandrino, N. Engheta, *Phys. Rev. B* **2007**, *75*, 155410.
[36] I. Liberal, N. Engheta, *Sci. Adv.* **2016**, *2*, e1600987.

